



# Dynamic light scattering microscopy sensing mitochondria dynamics for label-free detection of triple-negative breast cancer enhanced by deep learning

MEIAI LIN,<sup>1</sup> TING LIU,<sup>2</sup> YIXIONG ZHENG,<sup>1</sup> AND XIANGYUAN MA<sup>1,\*</sup>

<sup>1</sup>*Department of Biomedical Engineering, College of Engineering, Shantou University, Shantou 515063, China*

<sup>2</sup>*Department of Biology, College of Science, Shantou University, Shantou 515063, China*

\**maxiangyuan@stu.edu.cn*

**Abstract:** We established a deep learning-based dynamic light scattering (DLS) microscopy sensing mitochondria dynamic for label-free identification of triple-negative breast cancer (TNBC) cells. The capacity of DLS microscopy to detect the intracellular motility of subcellular scatters was verified with the analysis of the autocorrelation function. We also conducted an in-depth examination of the impact of mitochondrial dynamics on DLS within TNBC cells, employing confocal fluorescent imaging to visualize the morphology of the mitochondria. Furthermore, we applied the DLS microscopy incorporating the two-stream deep learning method to differentiate the TNBC subtype and HER2 positive breast cancer subtype, with the classification accuracy achieving 0.89.

© 2023 Optica Publishing Group under the terms of the [Optica Open Access Publishing Agreement](#)

## 1. Introduction

Breast cancer has been reported as the most commonly diagnosed cancer and has become the leading cause of cancer mortality in women globally [1,2]. Breast cancers can be categorized into different subtypes based on the expression of estrogen and progesterone receptors (ER/PR) and amplification of the human epidermal growth factor receptor 2 (HER2). Among these subtypes, triple-negative breast cancer (TNBC) stands out due to its absence of ER, PR, and HER2 expression and is characterized by relatively high aggressivity and metastasis. Unfortunately, TNBC remains the only breast cancer subtype still lacking effective treatment strategies and shows the worst prognosis in comparison to other subtypes.

Currently, the clinical diagnosis of breast cancer relies on several methods. Mammography is the most widely applied radiological examination for breast cancer detection, enabling the visualization of abnormal tissue features [3]. However, it has been observed that most TNBC tumors lack the abnormal features of breast cancer in mammograms, leading to inaccurate diagnoses [4]. Therefore, the TNBC detection commonly relies on the standard immunohistochemistry (IHC) approach to test the expression of ER, PR, and HER2 in biopsy samples. There is an increasing demand for developing novel methods, such as machine learning-based label-free imaging [5–7], and biomarkers that can provide unequivocal information about TNBC especially at early stages.

Label-free light scattering, including static light scattering and dynamic light scattering, has been developed as a noninvasive, promising method for disease diagnosis [8,9]. Static light scattering measures the angular distribution of the scattering intensity arising from the interaction of the light and specimens [10–12]. Therefore, it has been proposed to be applied in cell and tissue analysis for disease detection [13–15]. Dynamic light scattering (DLS) is the extension of static light scattering to detect the time-dependent scattered light fluctuation caused by the relative motion of particles [16]. DLS-based measurement of intracellular motion allows the label-free assessment of cell viability [17–21]. DLS microscopy has been demonstrated to

enable the study of cell dynamics in a non-invasive way since the motion of subcellular scatterers including organelles, cytoskeletal components, and even the cell membrane can cause the intensity fluctuations of the speckle [22,23]. For example, Rhonda D. and colleagues tested the built dynamic light scattering microscopy by imaging the living macrophage cells to reveal the different motility of intercellular zones [24]. Chulmin J. et. al. developed the field-based dynamic light scattering to examine the localized intracellular dynamics in human epithelial ovarian cancer cells [25]. Additionally, Suissa M. et. al. explored the global dynamics of the cell nucleus in the G1 phase of cell division using DLS [26]. However, there are no investigations about the application of DLS microscopy for the identification of breast cancer cells, especially the highly aggressive subtypes.

The TNBC cells appear complicated molecular changes at the cellular level, which has the potential to be identified using DLS. Mitochondria, the subcellular organelles that can provide the energy to maintain cell activities, have been demonstrated to make a significant contribution to the patterns of light scattering [11,27]. Moreover, mitochondria are continuously dynamic networks undergoing fission and fusion processes to regulate the development of cancer cells [28]. Notably, the mitochondria dynamics has been reported to be involved in the regulation of migration and invasion of breast cancer cells [28]. Recent studies have demonstrated that mitochondrial fission is extremely critical for the aggressiveness of TNBC cells as it can generate smaller mitochondria to accelerate cell proliferation and thus promote TNBC cell survival by inhibiting apoptosis. Therefore, the mitochondria dynamics has the potential to become a new therapeutic targeting for TNBC [29,30]. However, there is no available data to reveal the impact of mitochondria dynamics within the TNBC cell on DLS images.

In this manuscript, we develop a DLS microscopy for label-free identification of triple negative breast cancer cells assisted by a deep learning method. The setup enabling the acquisition of light scattering images with time evolution was constructed. The measurements of the fixed and living TNBC cells were performed to test the sensitivity of DLS microscopy for intracellular motility. To further examine the impact of the mitochondria dynamics of a TNBC cell on light scattering changes, the inhibition reagent of mitochondrial division inhibitor 1 (mdivi-1) was used to constrain the mitochondria fission. The result shows that the autocorrelation function of the DLS of the inhibited TNBC cells decays more slowly than that of normal TNBC cells, which suggests that DLS microscopy has the ability to differentiate the mitochondrial dynamics in a cell. Finally, the DLS microscopy was applied in combination with two-stream deep learning networks to classify the breast cancers of the TNBC subtype and HER2-positive breast cancer subtype. This proposed approach achieves high performances, with the area under the curve (AUC) of 0.95 and accuracy of 0.89. The result demonstrates that the deep-learning enhanced DLS microscopy enables the identification of the TNBC cells based on the intracellular motility.

## 2. Methods and materials

### 2.1. *Dynamic light scattering imaging microscopy enhanced by deep learning*

The schematic of the established dynamic light scattering microscopy enhanced by deep learning is shown in Fig. 1. A laser with a wavelength of 532 nm (New Industries Optoelectronics, China) is focused by a 4× objective lens (Olympus, Japan) and then coupled into a single-mode fiber (Thorlabs, USA) with the inner diameter of 50 μm that is held by a fiber clamp (Thorlabs, USA) equipped on an alignment stage (Thorlabs, USA). The guided laser beam outputs from another end of the fiber and illuminates the cell suspension on a microfluidic chip. Once the cells are excited by the laser, the corresponding scattered light varying with time can be detected by an objective lens under the defocusing mode and recorded by a CMOS camera (Thorlabs, USA) as output videos. In this work, a 10× objective lens with a numerical aperture of 0.25 is used. The objective lens works at the defocusing mode with a distance of about 150 μm away from the focusing plane. Both the range of the scatter angle  $\theta$ . and polar angle  $\varphi$  dependent on the

NA of the objective lens is from  $79^\circ$  to  $101^\circ$  [31]. The collected scattering light projects on the sensor chip of the camera as time-series patterns to output a video at 103.09 fps with about 10 s. Also, our dynamic light scattering microscopy is compatible with an inverted optical microscope (Leica, Switzerland).

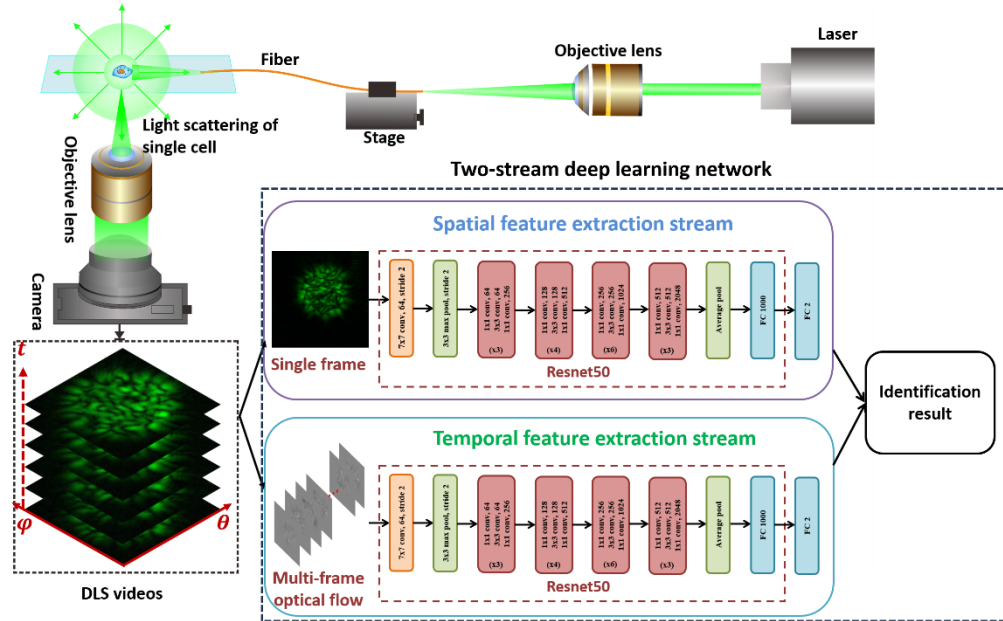


**Fig. 1.** Illustration of the established dynamic light scattering imaging microscopy enhanced by deep learning. The laser is forced by an objective lens and then coupled into an optical fiber, which can excite the cell suspension within the microfluidic chip. The scattering light of excited cells can be collected by an objective lens (10 $\times$ ) working at off-focusing distance of 150  $\mu\text{m}$ . The scattering light related with both the scatter angle  $\theta$  and polar angle  $\varphi$  can be captured by a camera at 103.09 Hz. The length of each output video is about 10 s. Finally, the two-stream deep learning network is applied to identify the breast cancer subtypes of the videos.

To investigate the applicability of DLS imaging for the differentiation of breast cancer subtypes, we develop a two-stream deep learning framework for cell identification. The two-stream deep learning framework utilizes the videos that are output from DLS microscopy as input and automatically classifies the subtypes of breast cancer. As shown in Fig. 1, the proposed deep learning framework is based on the effective two-stream architecture for video recognition tasks [32,33]. We modify and adjust the configuration of the two-stream architecture in order to obtain the suitable network structure for the cell identification task in this study. The proposed two-stream deep learning framework consists of two convolution paths. The first convolution path is the spatial feature extraction stream, which takes the first frame image of the cell video as input to extract the spatial features of the cell. The spatial information of the cell can help the differentiation of cells to some extent. The second path is temporal feature extraction stream, which captures the movement of the speckles inside the cell by analyzing the optical flow of the video. In DLS images, the movement of the speckles is highly correlated to the motion of subcellular structures of the cell. Hence, the temporal features play a crucial role in the identification of the cells. The specific design of the proposed network architecture is described in the following two paragraphs.

**Spatial feature extraction stream.** The spatial feature extraction stream aims to capture the spatial features of the cell. The spatial feature extraction stream is implemented using the Resnet-50 as backbone [34]. The Resnet-50 is a popular deep learning network due to its highly efficient features extraction ability in classification tasks. ResNet-50 is a convolutional neural network (CNN) consisting of 50 layers, where each layer performs convolutions on its input and applies batch normalization and ReLU activation. The architecture introduces residual blocks, incorporating shortcut connections that allow gradients to flow more effectively during training, thus enabling the training of deep networks with improved performance. In contrast to the original ResNet-50, we add a fully connected layer to restrict the number of output categories to 2. In addition, to obtain better classification performance, the pretrained version of Resnet-50 that trained on a dataset of over a million images from the ImageNet database is loaded and fine-tuned in this study.

**Temporal feature extraction stream.** The temporal feature extraction stream aims to captures the movement of the speckles inside the cell and also uses Resnet-50 as the backbone. But unlike the frequently-used Resnet-50, the input to the temporal feature extraction stream is formed by stacking optical flow images of the cell video. In order to explicitly describe the movement between video frames, the optical flow displacement fields between consecutive frames are calculated using the TV-L1 [35] optical flow estimation algorithm. Such input is able to make the cell identification easier, as the network is not required to implicitly estimate movement. In this study, we stack the horizontal component and vertical component of the optical flow of consecutive frames along channel dimension.

## 2.2. Sample preparation

The TNBC cell line MDA-MB-231 which is a highly metastatic subtype and HER-2 overexpressed cell line SKBR3 which is moderate in vitro metastatic potential were cultured as the standard protocols. For the cell fixation, the cultured cells were washed three times with phosphate-buffered saline (PBS) and digested with 1 mL trypsin for 2 min. The digestion was stopped by adding 3 mL culture media. Then the cell suspension was centrifuged at 1200 rpm for 3 min with the supernatant abandoned. About  $2 \times 10^5$ /mL cell suspensions were added into 24-well plates with 1 mL culture medium containing 4% paraformaldehyde to immobilize the cells. For the cell inhibition, the cell suspension was added with 1 mL mdivi-1 inhibitor (Beyotime, China) with 40  $\mu$ M concentration and incubated with 5% CO<sub>2</sub> for 15 min at 37°C. For the fluorescent staining of mitochondria and nucleus, the culture medium of 500  $\mu$ L was added to infiltrate the confocal dish bottom. Subsequently, about  $1 \times 10^5$ /mL cell suspension was added into the confocal dish and incubated for 48 hours with 5% CO<sub>2</sub> at 37°C. After 48 hours, the cells were washed 3 times with PBS. Then the fluorescent solution containing 0.1% Mito-Tracker Red (Beyotime, China) for mitochondria staining and 1% Hoechst 33342 solution (Beyotime, China) for nucleus staining was prepared and added to the confocal dish. After incubation for 15 min, the redundant dyes were moved by washing with PBS 3 times. Finally, 1 mL culture medium was added to make the cell suspension well for the confocal imaging.

## 3. Results and discussion

### 3.1. Dynamic light scattering microscopy sensing the intracellular motility of single cells

To investigate the impact of the intracellular organelle movement within TNBC cells on light scattering patterns to explore the feasibility of DLS microscopy for label-free detection of highly invasive breast cancer, the TNBC cell line MDA-MB-231 is used to perform experiments. The suspension of MDA-MB-231 cells fixed with methanal was prepared as the control group.

A single recorded video yields approximately 1000 time-series DLS images with a time interval  $\tau$  of 9.7 ms are extracted from a recording video, as presented in Fig. 2(a). To simplify the analysis, the region of interest (ROI) is defined as the area located at the central point of DLS image with 100 pixels  $\times$  100 pixels in length. The ROI images of the time-series DLS images form the ROI image stacks. The ROI image stacks (Fig. 2(b)) for both fixed and viable cells are collected for next analysis. The signal intensity as a function of time for a single pixel at the central point of ROI of light patterns is plotted in Fig. 2(c). It can be seen that the light scattering intensity of viable cell (red curve) presents more drastic fluctuation while the intensity curve of the fixed cell (blue curve) is relatively stable with a slight oscillation. The normalized temporal autocorrelation functions  $g(\tau)$  of the light scattering intensity with time evolution is calculated for the ROI patterns for both cases and plotted in Fig. 2(d). As expected, the autocorrelation function curve of fixed cells decays more rapidly to zero than that of viable cells, which means that the DLS intensity of fixed cells can be deemed as a stable signal. This is reasonable as the cellular activity of the fixed cells is compressed by the paraformaldehyde agent, the intracellular motion causing scattering fluctuation for fixed cells is restricted. Thus, this result demonstrates that the DLS microscopy is sensitive to the intracellular motility due to subcellular scatters such as the mitochondria and nucleus.

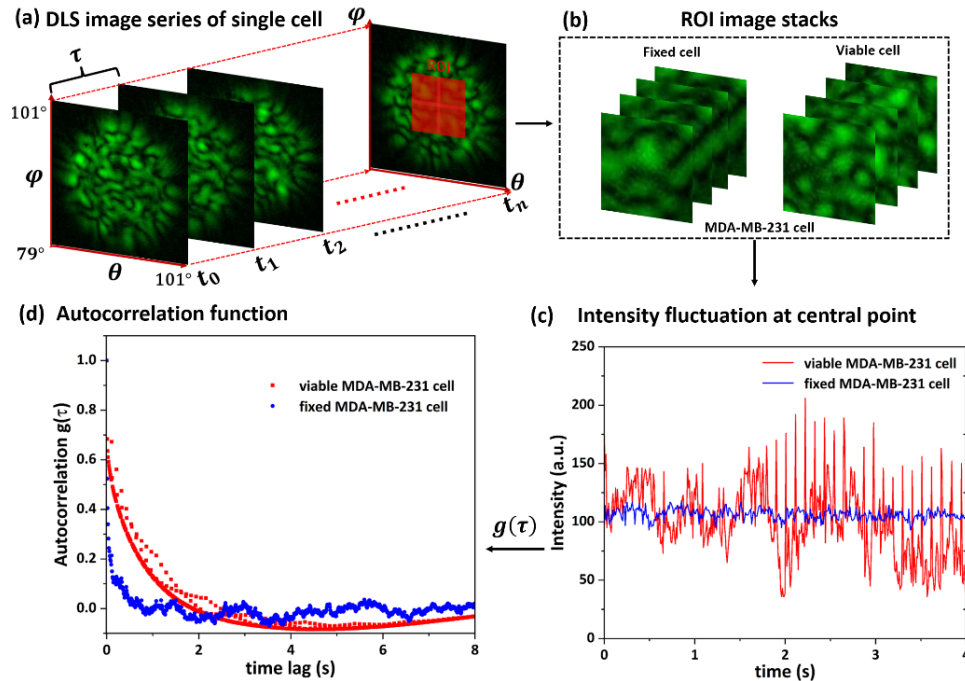


**Fig. 2.** Dynamic light scattering imaging of fixed and viable MDA-MB-231 cells. (a) The representative time-series DLS images of a single cell with the time interval of 9.7 ms. The ranges of scatter angle  $\theta$  and polar angle  $\phi$  are both from  $79^\circ$  to  $101^\circ$ . The ROI area located at the center point of each image is defined as 100 pixels  $\times$  100 pixels in length. (b) The ROI image stacks of each DLS image for both fixed and viable cells are built. (c) The normalized intensity of scattering light at the central point of DLS images for both groups varying with time. The blue curve and red curve denote the experimental results of fixed and viable cells, respectively. (d) The normalized average autocorrelation functions  $g(\tau)$  of the light scattering intensity over the ROI. The blue and red dots denote the experimental results of fixed and viable cells, respectively.



It is known that the mitochondria distributing within the cell are continuously dynamic networks undergoing fission and fusion processes to regulate the development of cancer cells [28]. It also has been proved that the mitochondria fission is controlled by the dynamin-related protein 1 (Drp1), which can form a ringlike structure to divide the mitochondria. Drp1 activity can be inhibited by using the reagent of mitochondrial division inhibitor 1 (mdivi-1), a small molecule that can inhibit the GTPase activity of DRP1 and thus restrict mitochondrial fission. [36]. In this work, to further explore the effect of mitochondria dynamics on DLS imaging of a single cell, the MDA-MB-231 cells are treated with mdivi-1 to constrict the mitochondria fission. There are 429 DLS videos of MDA-MB-231 cells and 113 videos of MDA-MB-231 cells with inhibitor collected for analysis. The representative time-series DLS images are collected and analyzed. Figure 3 shows the corresponding curves of the average autocorrelation function for both cases. The blue square dots and the red circular dots refer to the experimental data of MDA-MB-231 cells without and with mdivi-1, respectively. The fit curves of average autocorrelation function  $g(\tau)_s$  of both groups are also plotted as solid curves. The fit formula is given by

$$g(\tau)_s = A_0 * e^{(-A_1\tau)} + A_2$$

where  $A_1$  is the decay rate parameter that can report the motion of scattering centers [24]. The larger decay rate indicates the faster scatters motion, thus the smaller average sizes of scatters. To be specific, the average autocorrelation function  $g(\tau)_M$  of normal cells is  $g(\tau)_M = 0.689 * e^{(-1.462\tau)} - 0.064$  and that of cells with mdivi-1 inhibitor is  $g(\tau)_{M\_inhibitor} = 0.708 * e^{(-1.144\tau)} - 0.052$ . Obviously, the decay rate parameter  $1.426 \text{ s}^{-1}$  for normal cells is larger than  $1.144 \text{ s}^{-1}$  for the cells with inhibitor. This can be attributed to the fact that the inhibition of mitochondria fission results in the less discrete mitochondria in a cell, thus further decreasing the general subcellular scatter motion. From the result, we conclude that the mitochondria dynamics can cause detectable changes in the dynamic light scattering patterns.

### 3.2. Dynamic light scattering imaging of the breast cancer subtypes

To directly visualize the difference of the mitochondria distributions in the TNBC cell line MDA-MB-231 and HER-2 overexpressed cell line SKBR3, the fluorescent staining reagents of Mito-Tracker Red and Hoechst 33342 were used to stain the mitochondria and nuclei of the cells, respectively. Then the stained cells were imaged by confocal fluorescent microscopy (Zeiss, Germany). The sequential images of the mitochondria dynamics with 10 s intervals were obtained. Figure 4(a1) and (a2) display the representative images of mitochondrial distribution in an MDA-MB-231 cell at a time interval of 20 s. And the typical images for an SKBR3 cell are presented in Fig. 4(b1) and (b2). The magnified views show the selected regions of mitochondrial morphology for each cell. It can be clearly observed that the mitochondria in the MDA-MB-231 cells are more fragmented than in the SKBR3 cell in which the morphology appears interconnected network.

To quantitatively compare the difference in mitochondria dynamics between the two types of cells, the similarity analysis of images based on the structural similarity index measure (SSIM) method is performed. The result shows that the similarity parameter for the MDA-MB-231 cell and SKBR3 cell are 0.472 and 0.708, respectively. This indicates that mitochondria in the MDA-MB-231 cells change faster than those in the SKBR3 cells. The result is to be expected since the mitochondria are more fragmented in metastatic breast cancer cells of TNBC that express higher levels of total and active Drp1 protein as compared with non-metastatic HER-2 positive breast cancer cells [28].

Next, the DLS images of both cells are acquired and analyzed. A total of 372 SKBR3 cells and 429 MDA-MB-231 cells are used for analysis. Same as the method described previously, the DLS intensity fluctuating with time at the ROI central point from both cells is plotted in Fig. 4(c). It can be observed from the figure that the light scattering intensity of the MDA-MB-231 cell

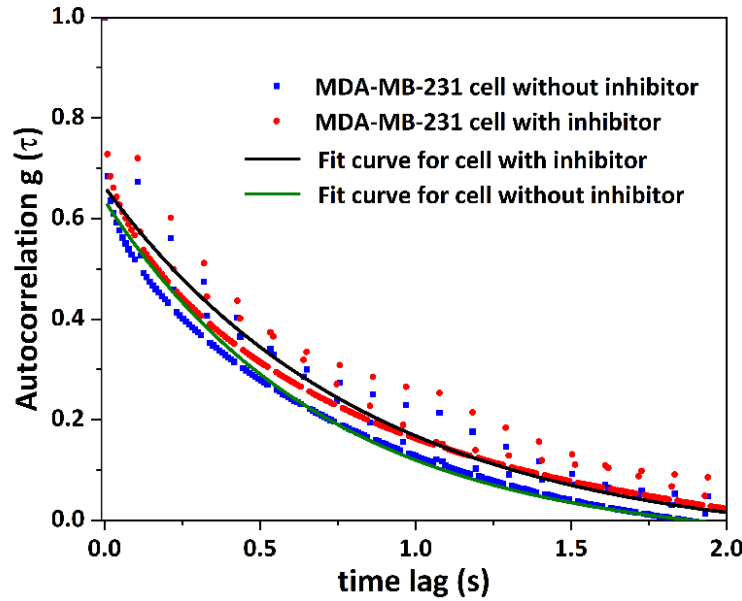


**Fig. 3.** The average autocorrelation functions of dynamic light scattering images of MDA-MB-231 cells with and without mitochondrial inhibitor. The blue and red dots denote the experimental results of normal MDA-MB-231 cells and MDA-MB-231 cells treated with the mdivi-1 inhibitor, respectively. The green and black solid lines refer to the fit curves of the normal cell and the cell treated with the mdivi-1 inhibitor, respectively. The average autocorrelation function  $g(\tau)_M$  for normal cells is given as  $g(\tau)_M = 0.689 * e^{(-1.462\tau)} - 0.064$  and for cells with mdivi-1 inhibitor is given by  $g(\tau)_{M\_inhibitor} = 0.708 * e^{(-1.144\tau)} - 0.052$ .

(the blue curve) fluctuates more dramatically than that of the SKBR3 cell (the red curve). The experimental results of the average autocorrelation function as well as the corresponding fit curves for both groups are shown in Fig. 4(d). The decay rate for MDA-MB-231 cells is  $1.426 \text{ s}^{-1}$  as mentioned above. In contrast, the average autocorrelation function for SKBR3 cells is given by  $g(\tau)_s = 0.789 * e^{(-1.195\tau)} - 0.066$  with the decay rate parameter  $A_1$  of  $1.195 \text{ s}^{-1}$ . It is obvious that the smaller decay rate parameter indicates the slower motion of the scatters in the SKBR3 cells, which has the potential to be used to classify the different subtypes of breast cancer cells. All of the results suggest that the dynamic light scattering microscopy enables the differentiation between the metastatic TNBC cancer and HER-2 positive breast cancer cells, based on the motion detection of subcellular structures such as the mitochondria.

### 3.3. Two-stream deep learning network for identification of the breast cancer subtypes

To further investigate the applicability of DLS imaging for the automatic differentiation of the breast cancer subtypes, the DLS microscopy enhanced by deep learning method was applied in the differentiation of TNBC cell line of MDA-MB-231 and HER-2 overexpressed cell line SKBR3. Using the DLS system we established, a dataset including 429 MDA-MB-231 cells and 372 SKBR3 cells were collected. The duration of each cell video was approximately 10 seconds and the frame rate was 103.09 fps. The original resolution of each frame was  $400 \times 400$ . We scaled the pixel value dynamic range to  $[-1.0, 1.0]$  and resized all the frames to  $224 \times 224$  to normalize the input videos.

To train and evaluate the performance of the deep learning framework we proposed in this study, we adopted five-fold cross-validation strategy. The MDA-MB-231 cells and SKBR3

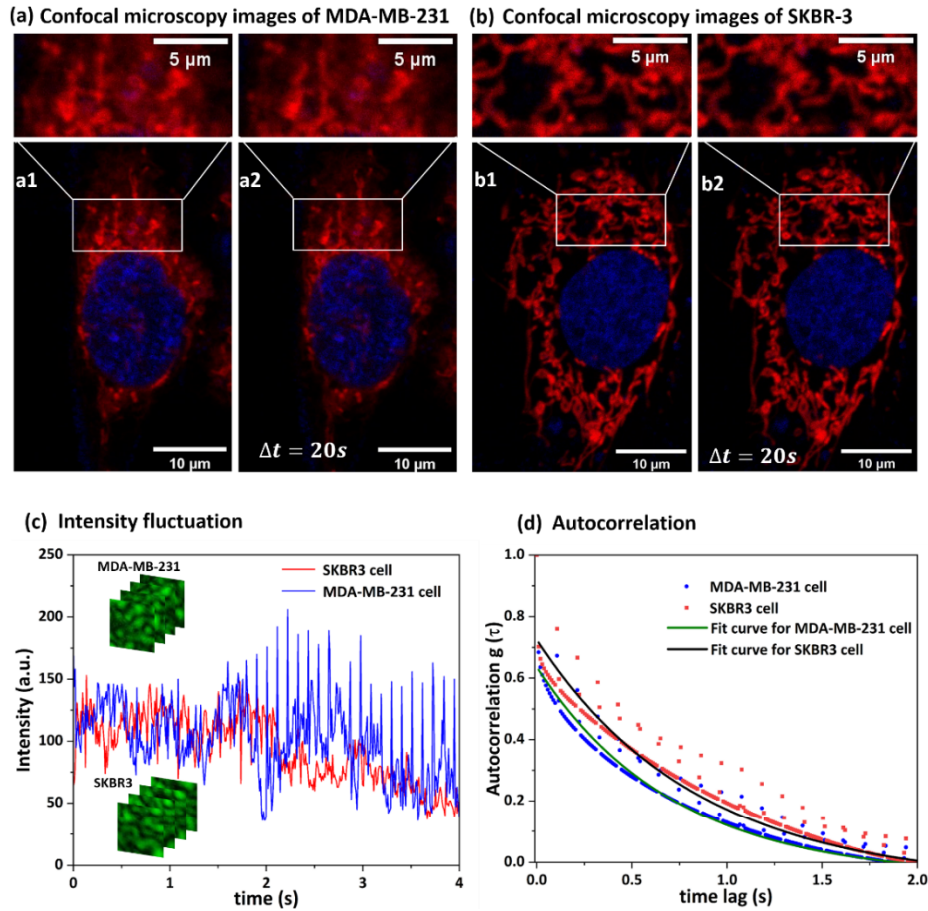


**Fig. 4.** Dynamic light scattering imaging of MDA-MB-231 and SKBR3 cells. (a) The confocal microscopy images of an MDA-MB-231 cell stained with Mito-Tracker Red for the mitochondria and Hoechst 33342 for the nucleus, respectively. Subfigure a1 and a2 show the cell images with a time interval of 20 seconds for an MDA-MB-231 cell. Magnified view of selected regions:  $14.7\ \mu\text{m} \times 6.9\ \mu\text{m}$  (length  $\times$  width). (b) The same results for SKBR3 cells. (c) The scattering light intensity at the central point of DLS images for both cells varying with time. The blue and red curves denote the results of MDA-MB-231 and SKBR3 cells, respectively. (d) The average autocorrelation functions of dynamic light scattering images of MDA-MB-231 cells and SKBR3 cells. The blue and red dots denote the experimental results of MDA-MB-231 cells and SKBR3 cells, respectively. The green solid line refers to the fit curve of MDA-MB-231 cells with the function of  $g(\tau)_M = 0.689 * e^{(-1.462\tau)} - 0.064$ . The black solid line is the result of SKBR3 cells and the function is  $g(\tau)_S = 0.789 * e^{(-1.195\tau)} - 0.066$ .



cells were first randomly partitioned into five folds. Subsequently, we randomly combined one MDA-MB-231 cell fold and one SKBR3 cell fold to form the five final folds. The deep learning model was trained five times. In each training cycle, we used four folds for training and validation, the remaining one fold was used for testing. The proposed deep learning was trained on an NVIDIA GeForce RTX 2080 Ti with 11-GB VRAM. We used the Adam [33] algorithm to optimize the weights of the deep learning networks by minimizing a binary cross-entropy loss function. The batch size was 32 and the learning rate was 0.0005. The model was trained with a fixed number of epochs at 50 and the model with best validation loss was selected as the best model.

In this study, we mainly aim to investigate the applicability of DLS imaging for the differentiation of different kinds of cells. Therefore, the static light scattering imaging based method was used as baseline for comparison. The static light scattering imaging based method used the single static image from static light scattering imaging microscopy as input. The single static image can offer valuable insights into cell composition and structural properties, but it lacks the capability to provide information regarding intracellular motion. Since the static light scattering imaging-based baseline method only uses the single static image as input, it only had the Resnet-50 spatial stream for feature extraction. Figure 5 shows examples of optical flow of MDA-MB-231 cell and SKBR3 cell. It can be seen that the movements of MDA-MB-231 cell and SKBR3 cell are quite different and it is easier to see the differences in the optical flow.

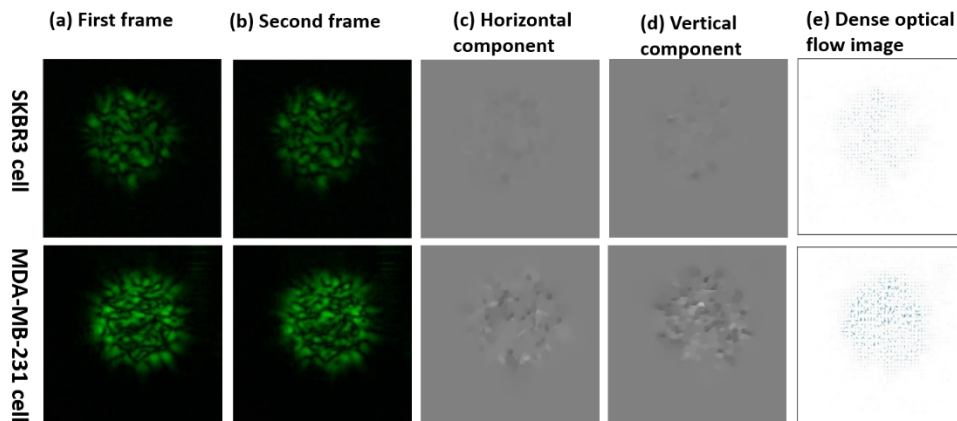


**Fig. 5.** Optical flow of SKBR3 cell (first row) and MDA-MB-231 cell (second row). (a) The first frame of a cell. (b) The second frame of a cell. (c) Horizontal component of the optical flow. (d) Vertical component of the optical flow. (e) Dense optical flows image.

Figure 6 shows the ROC curve results obtained from test set of the five-fold cross-validations for the two-stream deep learning framework and static light scattering based baseline method. It can be seen that the proposed two-stream deep learning framework was significantly better than the static light scattering imaging-based baseline method. The proposed method achieved an area under the curve (AUC) of 0.95, an accuracy of 0.89, a sensitivity of 0.91 and a specificity of 0.88. In comparison, the static light scattering based baseline method had corresponding measures of 0.75 for AUC, 0.66 for accuracy, 0.69 for sensitivity, and 0.64 for specificity. The results strongly supported the effectiveness of DLS imaging in differentiating MDA-MB-231 cells and SKBR3 cells.

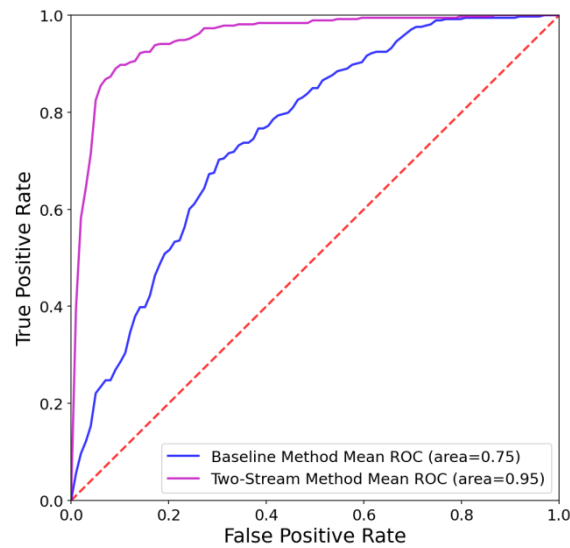


**Fig. 6.** The ROC curve results of the two-stream deep learning framework and static light scattering based baseline method.

#### 4. Conclusion

In this work, the two-stream deep learning network enhanced DLS microscopy sensing intracellular motion was developed aim at label-free identification of triple negative breast cancer cells. The feasibility of the DLS microscopy to detect the intracellular scatterer motion due to subcellular components such as the organelles was examined. From the comparison results of DLS images based on the autocorrelation function analysis, the scattered light pattern for the disabled cell barely changes with time and thus can be considered a stable signal. This finding confirms that our built DLS microscopy enables single-cell analysis at the subcellular level.

Furthermore, to explore the influences of mitochondria dynamics on DLS images, mitochondria fission was constrained by using the mdivi-1 inhibitor to control the Drp1 protein. The corresponding autocorrelation function of DLS images dropped slower as compared to the untreated cells. The decay rate parameter that can be used to indicate the motion degree of cellular scatters was calculated. The values were  $1.144 \text{ s}^{-1}$  and  $1.462 \text{ s}^{-1}$  for TNBC cells with and without mdivi-1, respectively. The results demonstrate that the detection sensitivity of DLS microscopy is sufficient to reveal the changes caused by the mitochondria dynamics in a cell.

Finally, DLS microscopy was applied to classify the different breast cancer subtypes. From the comparison of the sequential confocal fluorescent images of staining mitochondria, the mitochondrial morphologies in the TNBC cells exhibited more fragmented than in the HER-2-positive cells. Consistently, the decay rate parameter of the autocorrelation function for TNBC cells is relatively large, suggesting the active motion of the scatters in the TNBC cells. To further apply the DLS microscopy for the differentiation of breast cancer subtypes, we developed a two-stream deep learning network for classification of TNBC MDA-MB-231 cell and HER-2 enriched SKBR3 cell. The results further support the potential of DLS microscopy for distinguishing between different breast cancer subtypes.

**Funding.** 2020 Li Ka Shing Foundation Cross-Disciplinary Research Grant (2020LKSF07C); Guangdong Basic and Applied Basic Foundation (2020A1515111053, 2022A1515011566, 2023A1515011488).

**Disclosures.** The authors declare that there are no conflicts of interest related to this article.

**Data availability.** The data that support the findings of this study are available upon reasonable request.

## References

1. M. Arnold, E. Morgan, H. Rumgay, A. Mafra, D. Singh, M. Laversanne, J. Vignat, J. R. Gralow, F. Cardoso, S. Siesling, and I. Soerjomataram, "Current and future burden of breast cancer: Global statistics for 2020 and 2040," *Breast* **66**, 15–23 (2022).
2. H. Sung, J. Ferlay, R. L. Siegel, M. Laversanne, I. Soerjomataram, A. Jemal, and F. Bray, "Global cancer statistics 2020: GLOBOCAN estimates of incidence and mortality worldwide for 36 cancers in 185 countries," *CA Cancer J. Clin.* **71**(3), 209–249 (2021).
3. T. F. Mendes, L. D. Kluskens, and L. R. Rodrigues, "Triple Negative Breast Cancer: nanosolutions for a big challenge," *Adv. Sci.* **2**(11), 1500053 (2015).
4. B. E. Dogan and L. W. Turnbull, "Imaging of triple-negative breast cancer," *Ann. Oncol.* **23**(Suppl 6), vi23–vi29 (2012).
5. S. Farooq, M. Del-Valle, S. Santos, E. S. Bernandes, and D. M. Zezell, "Identifying breast cancer cell lines using high performance machine learning methods," in *Latin America Optics and Photonics (LAOP) Conference 2022*, Technical Digest Series (Optica Publishing Group, 2022), Tu5A.3.
6. S. Farooq, A. Caramel-Juvino, M. Del-Valle, S. Santos, E. S. Bernandes, and D. M. Zezell, "Superior Machine Learning Method for breast cancer cell lines identification," in *2022 SBFoton International Optics and Photonics Conference* (IEEE, 2022), pp. 1–3.
7. S. Farooq, M. Del-Valle, M. O. dos Santos, S. N. dos Santos, E. S. Bernandes, and D. M. Zezell, "Rapid identification of breast cancer subtypes using micro-FTIR and machine learning methods," *Appl. Opt.* **62**(8), C80–C87 (2023).
8. Z. A. Steelman, D. S. Ho, K. K. Chu, and A. Wax, "Light-scattering methods for tissue diagnosis," *Optica* **6**(4), 479–489 (2019).
9. V. Backman, M. B. Wallace, and L. T. Perelman, *et al.*, "Detection of preinvasive cancer cells," *Nature* **406**(6791), 35–36 (2000).
10. R. Xu, "Light scattering: A review of particle characterization applications," *Particuology* **18**, 11–21 (2015).
11. X. T. Su, C. Capjack, W. Rozmus, and C. Backhouse, "2D light scattering patterns of mitochondria in single cells," *Opt. Express* **15**(17), 10562–10575 (2007).
12. T. E. Matthews, M. Medina, J. R. Maher, H. Levinson, W. J. Brown, and A. Wax, "Deep tissue imaging using spectroscopic analysis of multiply scattered light," *Optica* **1**(2), 105–111 (2014).
13. X. T. Su, K. Singh, W. Rozmus, C. Backhouse, and C. Capjack, "Light scattering characterization of mitochondrial aggregation in single cells," *Opt. Express* **17**(16), 13381–13388 (2009).
14. X. T. Su, S. E. Kirkwood, M. Gupta, L. Marquez-Curtis, Y. Y. Qiu, A. Janowska-Wieczorek, W. Rozmus, and Y. Y. Tsui, "Microscope-based label-free microfluidic cytometry," *Opt. Express* **19**(1), 387–398 (2011).
15. L. Xie, Q. Liu, C. Shao, and X. Su, "Differentiation of normal and leukemic cells by 2D light scattering label-free static cytometry," *Opt. Express* **24**(19), 21700–21707 (2016).
16. P. Zakharov and F. Scheffold, "Advances in dynamic light scattering techniques," in *Light Scattering Reviews 4: Single Light Scattering and Radiative Transfer* (Springer, 2009), pp. 433–467.
17. L. F. Guerra, T. W. Muir, and H. Yang, "Single-particle dynamic light scattering: Shapes of individual nanoparticles," *Nano Lett.* **19**(8), 5530–5536 (2019).
18. D. D. Postnov, J. Tang, S. E. Erdener, K. Kılıç, and D. A. Boas, "Dynamic light scattering imaging," *Sci. Adv.* **6**(45), eabc4628 (2020).
19. Y. Park, M. Diez-Silva, D. Fu, G. Popescu, W. Choi, I. Barman, S. Suresh, and M. S. Feld, "Static and dynamic light scattering of healthy and malaria-parasite invaded red blood cells," *J. Biomed. Opt.* **15**(2), 020506 (2010).
20. R. Dzakpasu and D. Axelrod, "Dynamic light scattering microscopy. A novel optical technique to image submicroscopic motions. I: theory," *Biophys. J.* **87**(2), 1279–1287 (2004).
21. J. S. Lee, K. Eom, C. Polucha, and J. Lee, "Standard-unit measurement of cellular viability using dynamic light scattering optical coherence microscopy," *Biomed. Opt. Express* **9**(11), 5227–5239 (2018).
22. J. Lee, W. Wu, J. Y. Jiang, B. Zhu, and D. A. Boas, "Dynamic light scattering optical coherence tomography," *Opt. Express* **20**(20), 22262–22267 (2012).
23. G. Farhat, A. Miriampillai, V. X. Yang, G. J. Czarnota, and M. C. Kolios, "Detecting apoptosis using dynamic light scattering with optical coherence tomography," *J. Biomed. Opt.* **16**(7), 070505 (2011).
24. R. Dzakpasu and D. Axelrod, "Dynamic light scattering microscopy. A novel optical technique to image submicroscopic motions. II: Experimental applications," *Biophys. J.* **87**(2), 1288–1297 (2004).
25. C. Joo, C. L. Evans, T. Stepinac, T. Hasan, and J. F. de Boer, "Diffusive and directional intracellular dynamics measured by field-based dynamic light scattering," *Opt. Express* **18**(3), 2858–2871 (2010).
26. M. Suissa, C. Place, É. Goillot, B. Berge, and É. Freyssingeas, "Dynamic light scattering as an investigating tool to study the global internal dynamics of a living cell nucleus," *Europhys. Lett.* **78**(3), 38005 (2007).
27. J. R. Mourant, M. Canpolat, C. Brocker, O. Esponda-Ramos, T. M. Johnson, A. Matanock, K. Stetter, and J. P. Freyer, "Light scattering from cells: the contribution of the nucleus and the effects of proliferative status," *J. Biomed. Opt.* **5**(2), 131–137 (2000).
28. J. Zhao, J. Zhang, M. Yu, Y. Xie, Y. Huang, D. W. Wolff, P. W. Abel, and Y. Tu, "Mitochondrial dynamics regulates migration and invasion of breast cancer cells," *Oncogene* **32**(40), 4814–4824 (2013).
29. K. Weiner-Gorzel and M. Murphy, "Mitochondrial dynamics, a new therapeutic target for Triple Negative Breast Cancer," *BBA- Rev. Cancer* **1875**(2), 188518 (2021).

30. B. A. Humphries, A. C. Cutter, and J. M. Buschhaus, *et al.*, “Enhanced mitochondrial fission suppresses signaling and metastasis in triple-negative breast cancer,” *Breast Cancer Res.* **22**(1), 60 (2020).
31. M. Lin, X. Qiao, Q. Liu, C. Shao, and X. Su, “Light-sheet-based 2D light scattering cytometry for label-free characterization of senescent cells,” *Biomed. Opt. Express* **7**(12), 5170–5181 (2016).
32. K. Simonyan and A. Zisserman, “Two-stream convolutional networks for action recognition in videos,” in *Proceedings of the 27th International Conference on Neural Information Processing Systems - Volume 1* (MIT Press, Montreal, Canada, 2014), pp. 568–576.
33. C. Feichtenhofer, A. Pinz, and A. Zisserman, “Convolutional two-stream network fusion for video action recognition,” in *Proceedings of the IEEE Conference on Computer Vision and Pattern Recognition* (IEEE, 2016), pp. 1933–1941.
34. K. He, X. Zhang, S. Ren, and J. Sun, “Deep residual learning for image recognition,” in *Proceedings of the IEEE Conference on Computer Vision and Pattern Recognition* (IEEE, 2016), pp. 770–778.
35. J. S. Pérez, E. Meinhardt-Llopis, and G. Facciolo, “TV-L1 Optical Flow Estimation,” *Image Process. On Line* **3**, 137–150 (2013).
36. S. L. Archer, “Mitochondrial dynamics—mitochondrial fission and fusion in human diseases,” *N. Engl. J. Med.* **369**(23), 2236–2251 (2013).